

SUPPORTING INFORMATION

Scalably synthesized environmentally benign, aqueous-based binary nanoparticle inks for $\text{Cu}_2\text{ZnSn}(\text{S},\text{Se})_4$ photovoltaic cells achieving over 9% efficient

Ki-Joong Kim,^{abef} Changqing Pan^{ab}, Shalu Bansal,^c Rajiv Malhotra,^c Dae-Hwan Kim,^d Chih-Hung Chang,^{*ab}

^aSchool of Chemical, Biological & Environmental Engineering, Oregon State University, Corvallis, Oregon 97331, United States.

^bOregon Process Innovation Center, Advanced Technology and Manufacturing Institute, Corvallis, Oregon 97330, United States.

^cDepartment of Mechanical Engineering, Oregon State University, Corvallis, Oregon 97331, United States.

^dConvergence Research Center for Solar Energy, Daegu Gyeongbuk Institute of Science & Technology (DGIST), Daegu 42988, South Korea.

^eNational Energy Technology Laboratory (NETL), U.S. Department of Energy, 626 Cochran Mill Road, Pittsburgh, Pennsylvania 15236, United States.

^fAECOM, P.O. Box 618, South Park, Pennsylvania 15216, United States.

*Corresponding author: C-H.C. (chih-hung.chang@oregonstate.edu)

Figures

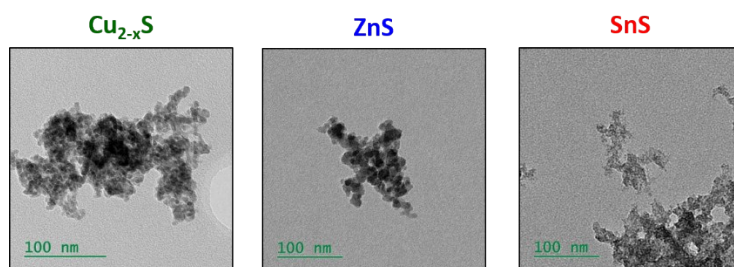


Figure S1. TEM images of each binary NPs synthesized by a continuous flow precipitation method.

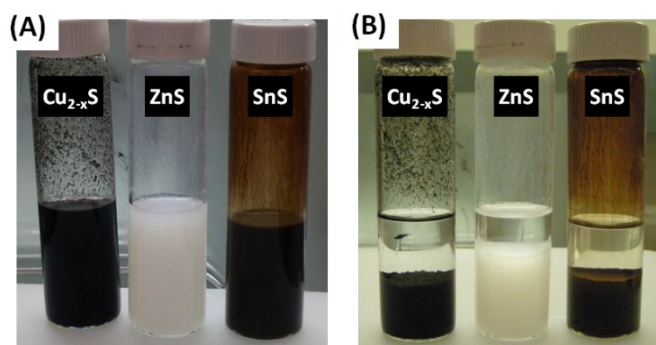


Figure S2. (A) As-synthesized binary NPs within an aqueous solution and (B) after washing and dispersing in EtOH at room temperature for 1 day.

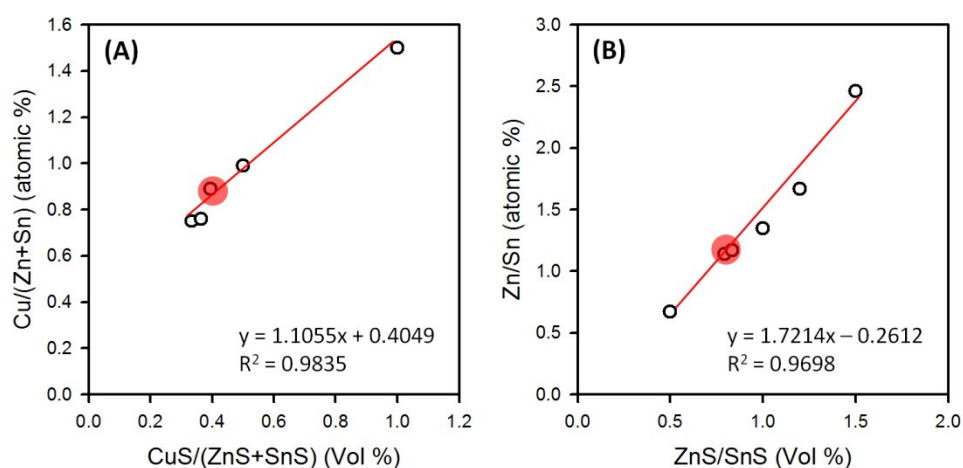


Figure S3. Determination of (A) $\text{Cu}/(\text{Zn}+\text{Sn})$ and (B) Zn/Sn ratios in the precursor mixtures of binary NPs. The circles in the figures were targeted in this study.

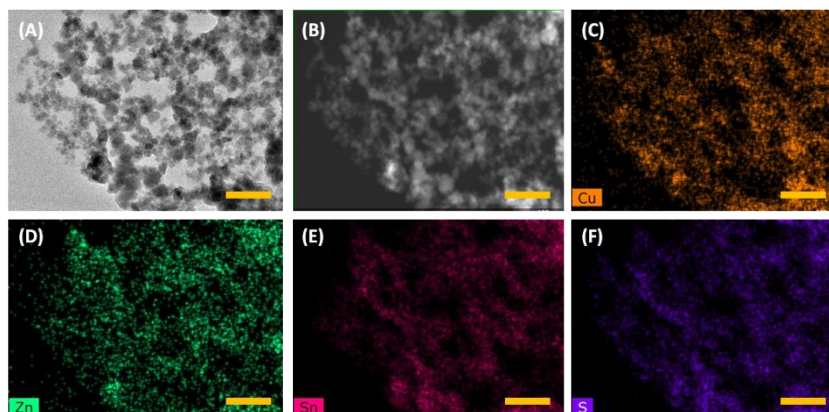


Figure S4. (A) TEM and (B) HAADF-STEM images of the binary NP-based ink. (C-F) EDS mappings for the compositional distribution of the ink. Scale bar is 100 nm.

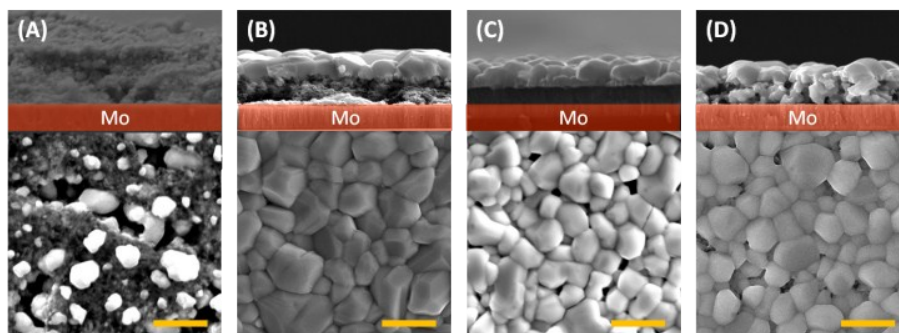


Figure S5. Top and cross-sectional SEM images of the selenized CZTSSe films at 530 °C for 30 min after pre-annealed at 350 °C in air using a binary NPs-based ink solution mixed with different additives. (A) Without additives, (B) with pure MEA, (C) with pure PVP, and (D) with MEA + PVP in a solution of binary NPs. Scale bar is 3 μm .

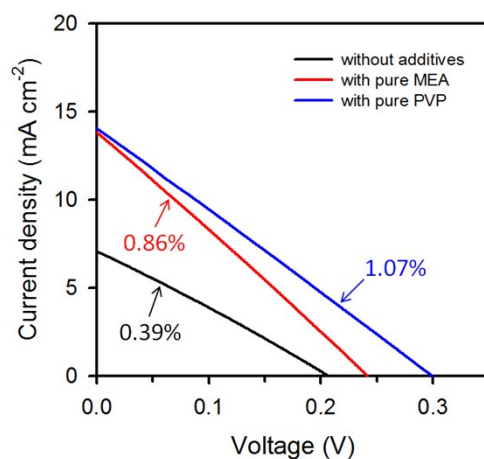


Figure S6. The current-voltage (I-V) characteristics under AM1.5 illumination of the CZTSSe PV devices without additives (black), with pure MEA (red), and with pure PVP (blue).

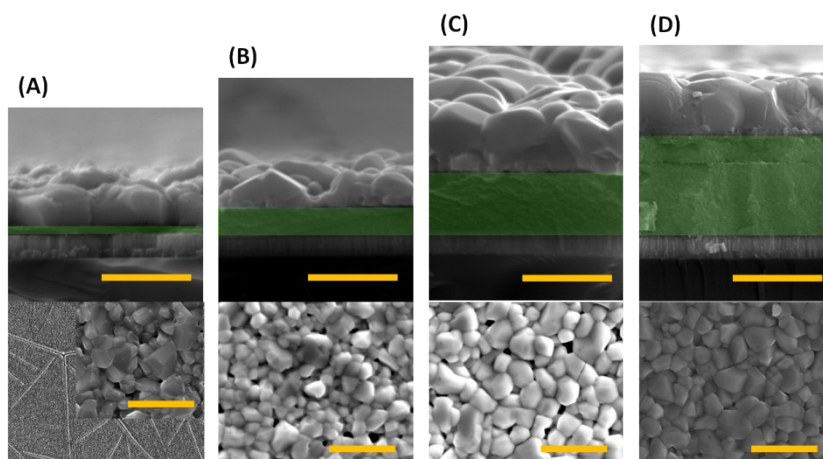


Figure S7. Effect of spin-coating/annealing cycles of precursor ink without MEA on the formation of CZTSSe films pre-annealed at 350 °C and selenized at 530 °C for 30 min. (A) 3 cycles, (B) 5 cycles, (C) 7 cycles, and (D) 9 cycles. Scale bars are 3 μm (top) and 5 μm (bottom), respectively.

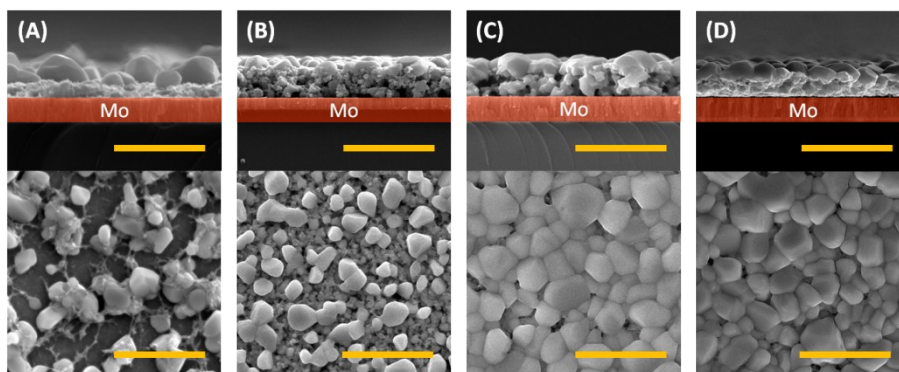


Figure S8. Effect of MEA amount in precursor ink on the formation of CZTSSe films pre-annealed at 350 °C and selenized at 530 °C for 30 min. (A) 0.1 mL-MEA, (B) 0.3 mL-MEA, (C) 0.5 mL-MEA, and (D) 0.7 mL-MEA. Scale bar is 5 μm .

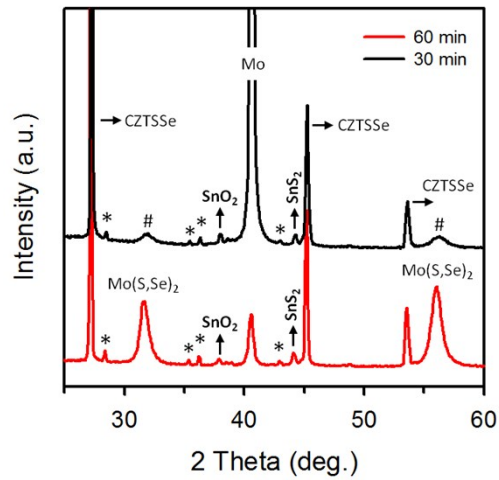


Figure S9. XRD patterns of CZTSSe films from the precursor film pre-annealed at 400 °C in air. In spite of selenization time increase, the SnO_2 and SnS_2 peaks remain and a thicker Mo(S,Se)_2 layer was observed. When hydrogen was used to remove the oxygen in the selenization process, films peeled-off from the Mo substrate.

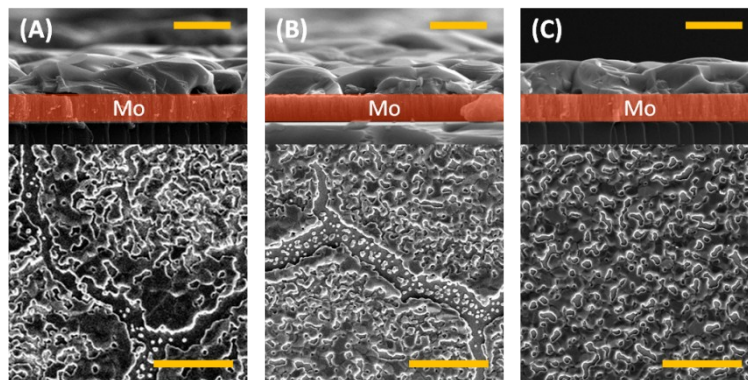


Figure S10. Effect of pre-annealing temperature in air on the formation of CZTSSe films selenized at 530 °C for 30 min. (A) 250 °C, (B) 300 °C, and (C) 350 °C. Further increasing temperature \sim 400 °C caused films peeling after the selenization process. Scale bars are 3 μm (top) and 30 μm (bottom), respectively.

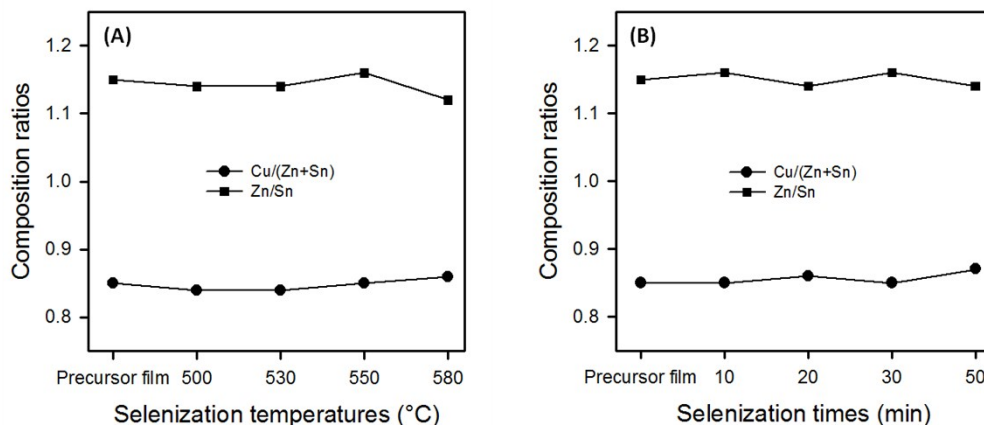


Figure S11. Elemental composition of the CZTSSe films selenized at different (A) temperatures and (B) times.

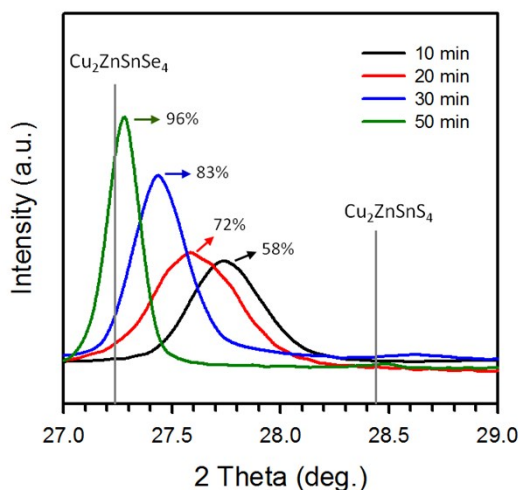


Figure S12. Selenization of precursor film pre-annealed at 350 °C in air for different times. The systematic shift in the main (112) peak toward smaller 2θ values over time indicates a higher Se content in the CZTSSe films with increased selenization times. From the position of the (112) peaks, the overall %Se were calculated to be 58, 72, 83 and 96% for 10, 20, 30, 50 min, respectively.

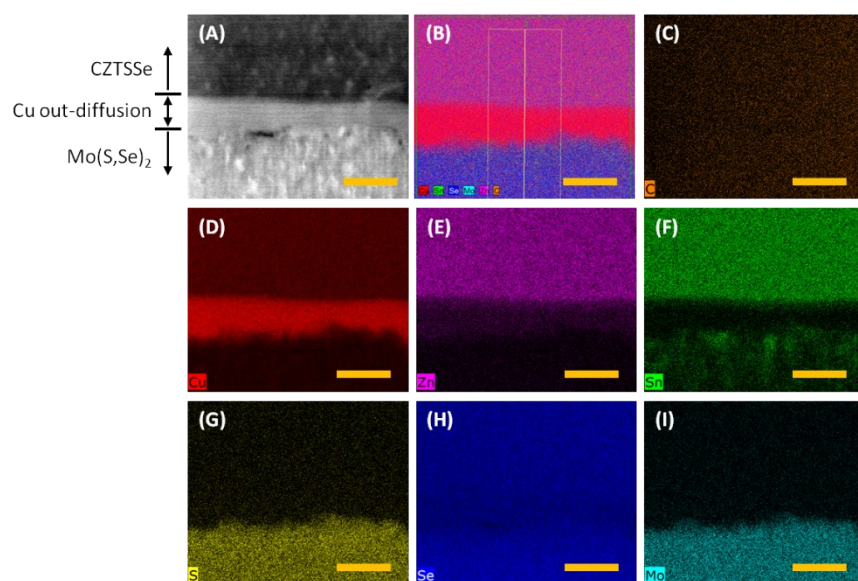


Figure S13. EDS mapping of lower CZTSSe film. (A) Cross-sectional HAADF-STEM image of the integrated film (CZTSSe/Mo(S,Se)₂/Mo) milled by a FIB technique and (B–I) EDS mappings for the compositional distribution of the CZTSSe film. Scale bar is 100 nm.

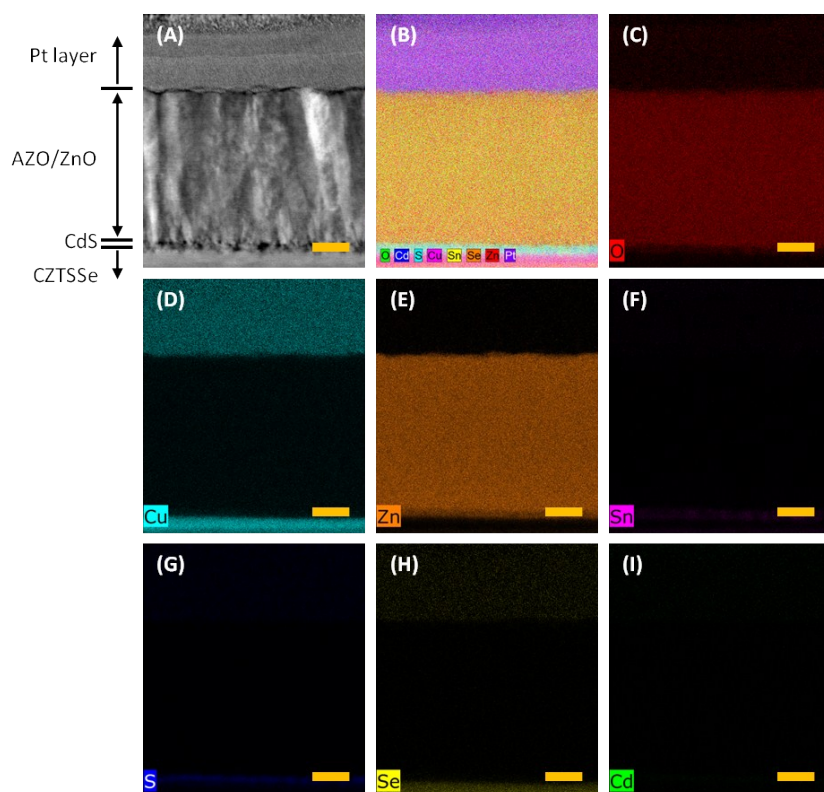


Figure S14. EDS mapping of upper CZTSSe film. (A) Cross-sectional HAADF-STEM image of the integrated film (CZTSSe/CdS/ZnO/AZO) milled by a FIB technique and (B–I) EDS mappings for the compositional distribution of the CZTSSe film. Scale bar is 100 nm.

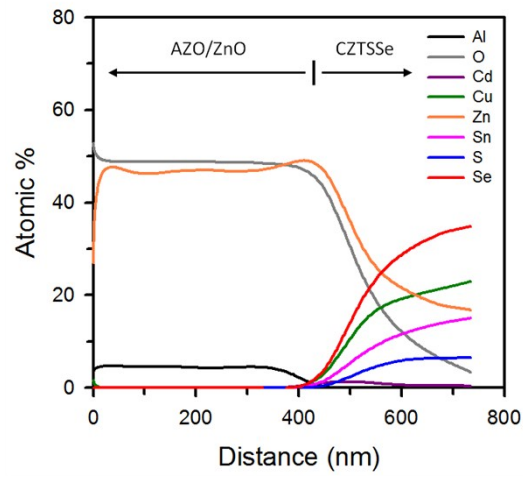


Figure S15. XPS depth profile of upper layer of 9.08% CZTSSe PV device.

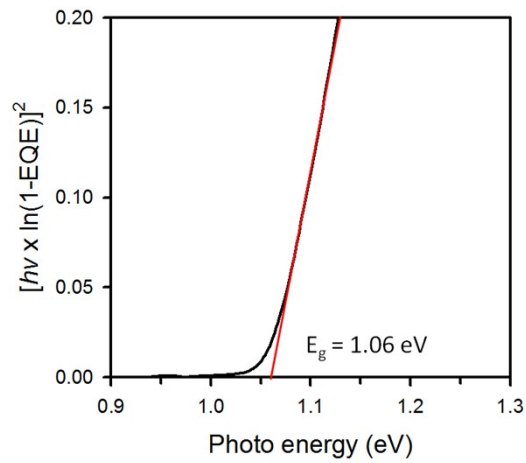


Figure S16. Band gap of 9.08% PV device estimated using $[\ln(1 - EQE)]^2$ versus the photon energy (eV), as well as the inflection of the EQE curve. The estimated band gap is 1.06 eV.